PNAS RESEARCH ARTICLE | PHYSICS

Direct observation of the collective modes of the charge density wave in the kagome metal CsV_3Sb_5

Doron Azoury[a,1], Alexander von Hoegen[a,1], Yifan Su[a], Kyoung Hun Oh[a], Tobias Holder[b], Hengxin Tan[b], Brenden R. Ortiz[c], Andrea Capa Salinas[c], Stephen D. Wilson[c], Binghai Yan[b], and Nuh Gedik[a,2]

Edited by Angel Rubio, Max-Planck-Institut fur Struktur und Dynamik der Materie, Hamburg, Germany; received May 23, 2023; accepted July 31, 2023

A recently discovered group of kagome metals AV_3Sb_5 (A = K, Rb, Cs) exhibit a variety of intertwined unconventional electronic phases, which emerge from a puzzling charge density wave phase. Understanding of this charge-ordered parent phase is crucial for deciphering the entire phase diagram. However, the mechanism of the charge density wave is still controversial, and its primary source of fluctuations—the collective modes—has not been experimentally observed. Here, we use ultrashort laser pulses to melt the charge order in CsV_3Sb_5 and record the resulting dynamics using femtosecond angle-resolved photoemission. We resolve the melting time of the charge order and directly observe its amplitude mode, imposing a fundamental limit for the fastest possible lattice rearrangement time. These observations together with ab initio calculations provide clear evidence for a structural rather than electronic mechanism of the charge density wave. Our findings pave the way for a better understanding of the unconventional phases hosted on the kagome lattice.

kagome | ultrafast | ARPES | collective modes | charge density wave

Highly correlated systems may exhibit a complex electronic phase diagram, where multiple phases are intimately related, and can be thought of as intertwined phases. In some cases, such as high-temperature superconductors (1), understanding the nature of individual phases is insufficient, and knowledge of the transition from one phase to another is crucial in order to understand the physics of these systems. Such an array of intertwined phases were recently discovered in a class of vanadium-based kagome metals AV_3Sb_5 (A = K, Rb, Cs) (2–10). In these compounds, all the phases emerge from a parent phase of a charge density wave (CDW). In the most simple case, a CDW forms when regions of the Fermi surface with high density of states can be connected by the same nesting wavevector. This leads to a spatial modulation of the electron density and concomitant distortion of the crystal lattice (Fig. 1*C*), which lowers the crystal's energy and opens an energy gap. Recent studies have revealed the properties of the CDW phase in AV_3Sb_5 (3–8). Specifically, the unit cell doubles along both in-plane directions, with nesting vectors connecting the high density of states at the van Hove singularities, located at the M points on the Brillouin zone boundary. This is also where the CDW gap opens, while the band near the Γ point remains gapless (11). The CDW in AV_3Sb_5 was shown to be very amenable to external perturbation such as hydrostatic pressure (10, 12–14) or doping (15) and recent studies revealed an additional weak reconstruction along the out-off-plane direction (5, 16, 17). Additionally, the observations of chirality in the CDW phase (4, 18, 19), the absence of acoustic phonon softening (20) and a pronounced anomalous Hall effect (21–23) suggest an electronic origin of the charge order in AV_3Sb_5. However, the underlying mechanism that forms the CDW was not directly resolved so far. In order to better understand the complete phase diagram, and how individual phases relate to one another, determining the parent phase mechanism is a crucial step.

To address these open questions, time-resolved studies were proven to be a powerful tool to resolve otherwise inaccessible aspects of interactions by measuring a response to impulsive excitation. These techniques are sensitive to collective dynamics of a condensed matter system, including the melting of long-range order and the fundamental modes of a CDW (24–26). The latter manifest as collective oscillations of the electronic density modulation, or a sliding motion of the CDW, known as the amplitude and phase modes, respectively (see illustrations in Fig. 1 *C* and *D*). These modes typically constitute the lowest energy collective excitations (GHz to few THz) of the system. As such, they define a distinctive time scale, imposing a minimum value of the structural response time in a photoinduced phase transition typically on the order of a few hundred femtoseconds (fs). Conversely, if the melting is purely electronic, it takes place on a much faster, electronic,

Significance

Elucidating the underlying mechanism of a phase transition is crucial for the comprehension of complex phase diagrams in quantum materials. A recently discovered class of vanadium-based kagome metals features an array of intertwined phases, including a charge density wave and superconductivity. However, the way these phases form and how they relate to one another are still central open questions. Here, we use time-, momentum-, and energy- resolved measurements for directly probing the charge order energy gap in CsV_3Sb_5. We identify the collective modes of the charge density wave and determine its mechanism. Our results establish the dominant role of electron–phonon coupling in the parent phase of these kagome systems, which is a key for our understanding of their complex phase diagram.

Author contributions: N.G. supervised the study; D.A., A.v.H., Y.S., and K.H.O. performed the trARPES measurements; A.v.H. and D.A. analyzed the data; T.H., H.T., and B.Y. performed the DFT calculations; B.R.O., A.C.S., and S.D.W. performed the crystal growth; All authors discussed the results and contributed to the final manuscript.

The authors declare no competing interest.

This article is a PNAS Direct Submission.

[1]D.A. and A.v.H. contributed equally to this work.

[2]To whom correspondence may be addressed. Email: gedik@mit.edu.

This article contains supporting information online at https://www.pnas.org/lookup/suppl/doi:10.1073/pnas.2308588120/-/DCSupplemental.

Published September 25, 2023.

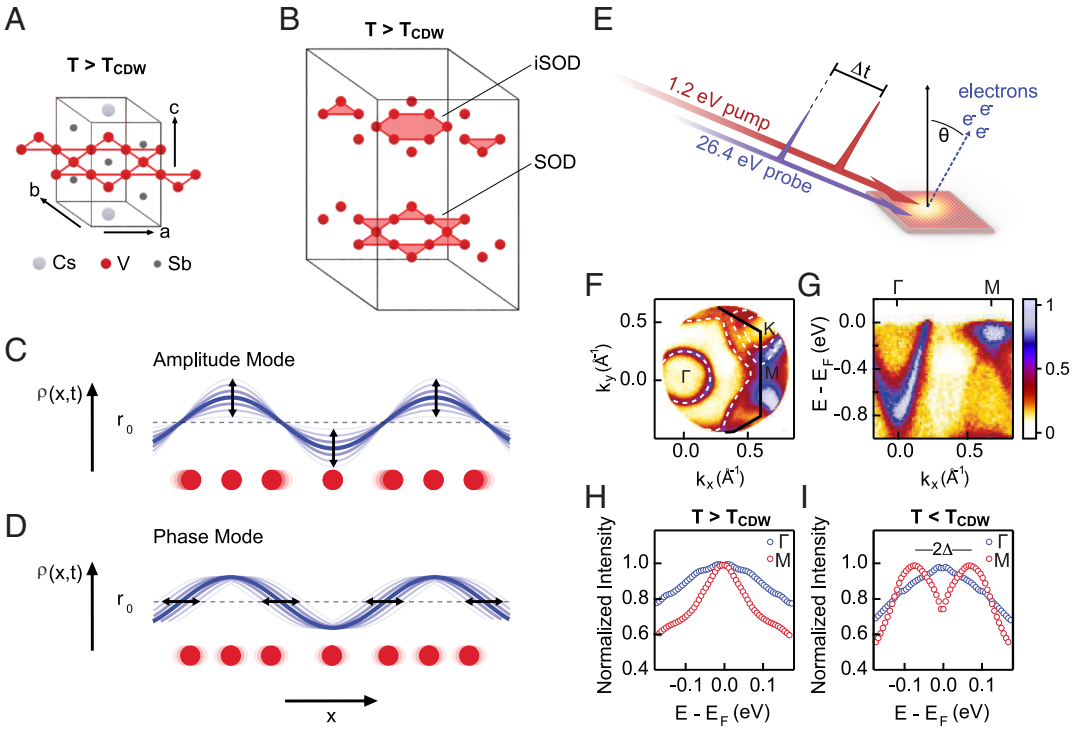

Fig. 1. Charge density wave in CsV_3Sb_5. (*A*) Crystal structure of CsV_3Sb_5 above the CDW transition temperature T_{CDW}. (*B*) Schematic of the two stacked distortion types in CsV_3Sb_5, Star-of-David (SOD) and inverse Star-of-David (iSOD) in the charge density wave phase below T_{CDW}. (*C* and *D*) Illustration of the collective motion induced by amplitude and phase modes in a CDW system, where the red spheres and the blue curves correspond to the lattice and charge density, respectively. (*E*) Schematic description of the trARPES experiment. A synchronized pump–probe pulse pair excites the sample, and the emitted photoelectrons are detected by a time-of-flight electron detector that resolves their energy and momentum. (*F* and *G*) Static ARPES spectra, showing a constant energy cut at the Fermi level (*F*) and energy–momentum cut along the Γ-M high-symmetry line (*G*). The characteristic spectral features of CsV_3Sb_5 are identified around the Γ point (parabolic band), M point (Van Hove singularity) and the Fermi surface shows good agreement with a superimposed DFT calculation (white dashed line in *F*). (*H* and *I*) Symmetrized energy density curves, extracted at the Γ band and M point, above and below T_{CDW}, showing the opening of a gap 2Δ at the M point.

femtosecond time scale. Therefore, the combined knowledge of the response time and the collective modes allows the identification of the dominant interaction driving the phase transition. Experimentally, amplitude and phase modes in CDWs are routinely observed using Raman and infrared spectroscopy, yet, eluded detection in AV_3Sb_5 so far (22, 27–30). To accurately describe and predict the phase transitions in any condensed matter system a comprehensive knowledge of the collective modes is required, leaving a large gap in our understanding of the AV_3Sb_5 kagome system.

Here, we perform time- and angle-resolved photoemission spectroscopy (trARPES) to study the dynamics of the CDW in CsV_3Sb_5. trARPES gives access to the nonequilibrium electronic band structure during a photoinduced phase transition on a femtosecond timescale. This time-, energy-, and momentum-resolved approach allows us to directly probe the CDW gap, and observe nonthermal melting of the charge order as well as its ultrafast recovery (31–33). The ultrafast photoexcitation impulsively excites coherent oscillations throughout the electronic band structure, which agree well with known CDW-induced phonons. Yet, trARPES unfolds the momentum integrated information obtained in other techniques, allowing for the assignment of band-selective electron–phonon coupling (34–36). Analysis of the time-dependent signal within the CDW gap at the M-point reveals two additional modes, so far unobserved by any other spectroscopic method, which differ from the detected phonons by showing a frequency softening at elevated fluences. In combination with ab initio density functional theory (DFT) calculations, we identify these modes as the amplitude modes of the three-dimensional CDW in CsV_3Sb_5. Finally, the measurement of the charge-order melting time together with the detection of the amplitude modes establish a complete basis to determine the interaction that dominates the CDW phase in CsV_3Sb_5 as structural.

Results

CsV_3Sb_5 exhibits a quasi-two-dimensional crystal structure (space group P6/mmm) of alternately stacked alkali and V–Sb planes. Each V–Sb plane hosts a two-dimensional kagome network of V atoms in which the hexagonal centers are occupied by Sb atoms. The additional out-of-plane Sb atoms form two honeycomb lattices above and below the V kagome network (Fig. 1*A*). Below a temperature of $T_{CDW} = 94$ K, the crystal undergoes a CDW phase transition, and the unit cell doubles along all in-plane directions. Recent diffraction and static ARPES studies suggest an additional lattice reconstruction along the out-of-plane direction: The lattice relaxes into a mixture of $2 \times 2 \times 2$ and $2 \times 2 \times 4$ reconstructions through a so-called star-of-David (SOD) and inverse star-of-David (iSOD) distortions of the vanadium atoms on adjacent layers (Fig. 1*B*) (3, 5, 17). Static ARPES measurements revealed the equilibrium band structure showing features associated with the kagome network: Dirac fermions at the K band and Van Hove singularities at the M point of the Brillouin zone. The CDW phase transition renormalizes the band structure and opens a highly anisotropic gap around the M point. Fig. 1*F* shows a static ARPES measurement of the Fermi surface in CsV_3Sb_5, taken at $T = 35\,\text{K} < T_{CDW}$,

as captured by our time-of-flight based ARPES detection (*SI Appendix*). The high-symmetry points (Γ, K, and M) are marked on two different cuts (Fig. 1 *F* and *G*). Energy distribution curves (EDC), extracted at the pocket around the Γ point and at the M point (Fig. 1 *H* and *I*) show the opening of a gap at the M point while the Γ band remains metallic. Our static ARPES data are consistent with all previous studies (37–40).

To investigate the CDW in CsV_3Sb_5, beyond what is possible within the static approach, we use an ultrashort near-infrared (1.2 eV) pump pulse to transiently perturb the CDW order and a second, time delayed, extreme ultraviolet (26.4 eV) probe pulse to stimulate photoemission of electrons (Fig. 1*E*). We scan the delay (Δt) between the pump–probe pair, and perform an ARPES measurement for each delay, to obtain the nonequilibrium electron band structure during the photoinduced phase transition. To effectively visualize the transient changes of the band structure, we treat the unperturbed spectra at negative delay as a baseline and plot the relative changes in blue (negative) and red (positive) for selected time delays (Δt = 0 ps, 1 ps, and 5 ps) in Fig. 2. Fig. 2 *A*–*C* shows the relative changes

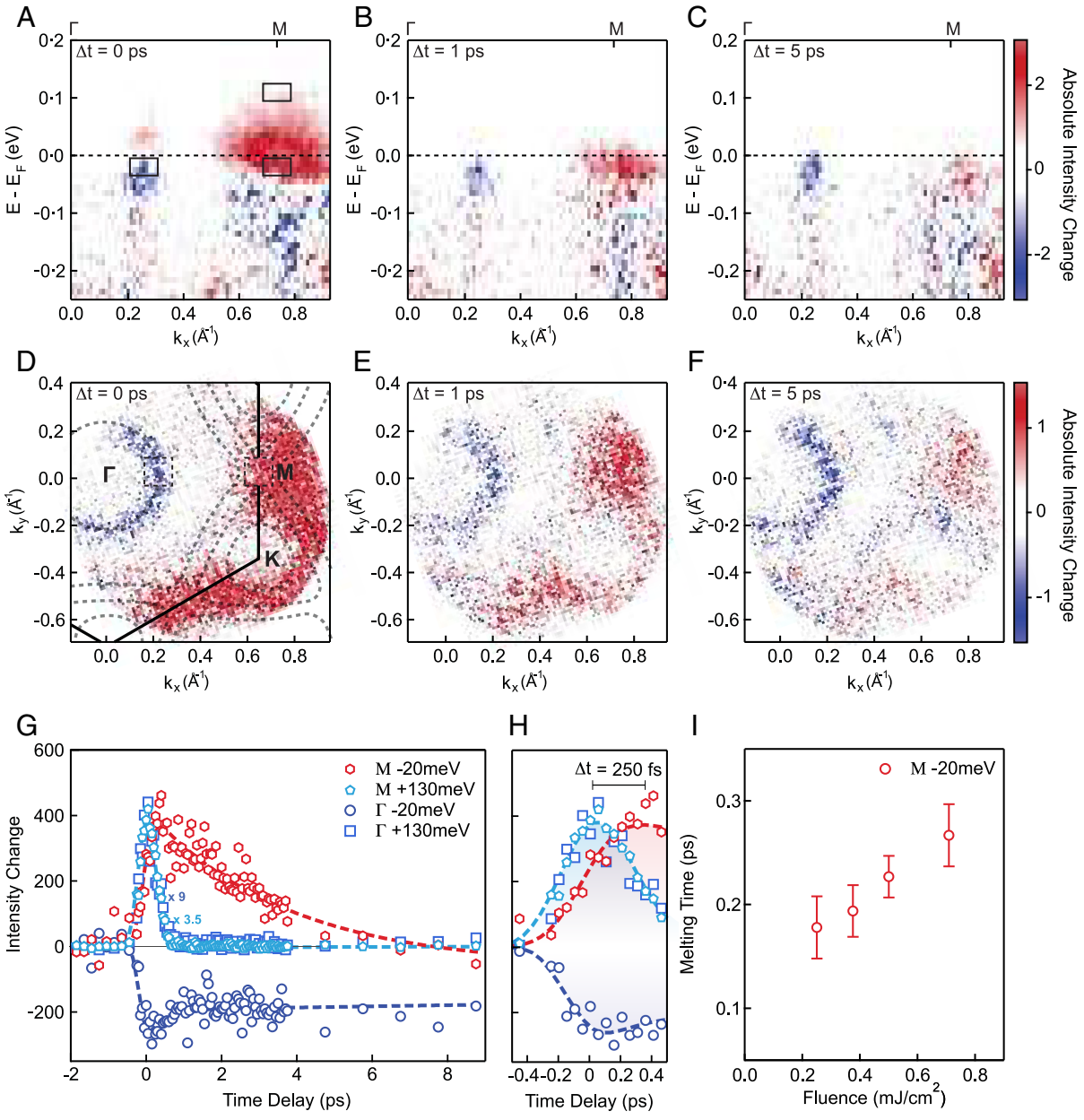

Fig. 2. Charge density wave dynamics in CsV_3Sb_5. (*A*–*F*) Differential spectra for an energy–momentum cut along the Γ-M high-symmetry line (*A*–*C*) and a constant energy cut at $E = E_F - 20$ meV (*D*–*F*), for three different delays (t = 0 ps, 1 ps, 5 ps). The spectral gain (loss) signal is marked in red (blue). The transition between loss and gain signal at the Γ metallic band is symmetric with respect to the Fermi level (dashed black line in *A*–*C*), whereas the gap region at the M point shows substantial gain below the Fermi level. In (*D*–*F*), the gain signal allows the identification of the bands that host the CDW gap. A sketch of the band structure is superimposed for reference. (*G*) Spectral intensity as a function of time delay, extracted from the regions marked in (*A*). The metallic Γ band (dark blue) shows a fast depletion followed by partial recovery. The excited states at both the M point (turquoise) and Γ band show a fast rise, synchronized with the depletion peak of the Γ band below the Fermi level, and a fast decay. The in-gap intensity at the M point (red) shows a slower rise time, corresponding to the melting time of the CDW, followed by a 4-ps recovery time. The dashed lines correspond to a double-exponential fit. (*H*) A close-up over the onset of the interaction, showing a 250-fs delay of the in-gap signal. (*I*) CDW melting time as a function of pump fluence. The data in (*A*–*H*) correspond to excitation fluence of 0.5 mJ/cm^2.

along the energy–momentum cut between the Γ and M points including both the metallic Γ-band and the CDW gap at M. As expected from a metallic band, the transition between the loss and gain signal at the Γ band is found at the Fermi energy (E_F) as a result of the transiently increased electronic temperature following the laser excitation. At the M point, the transition between loss and gain is shifted to below the Fermi energy. This is the transient closing of the CDW gap and filling in of the previously unoccupied states inside the gap region, leading to spectral gain below the Fermi energy (41). Following the intensity contour therefore allows us to visualize the energy–momentum cross-section of the CDW gap itself. Above E_F, at both Γ and M bands we observe the population of excited states, which completely decay within 1 ps (Fig. 2 *A* and *B*), while the gap remains closed, and reopens at later times (Fig. 2 *B* and *C*). The constant energy cuts (E = −20 meV), spanned by the two orthogonal momentum directions k_x and k_y shown in Fig. 2 *D*–*F*, provide complementary information. Here, we can directly identify the bands that host the CDW gap by using differential contrasting: a gain signal is associated with the gap-related bands, whereas a loss signal is associated with a normal metallic band. We repeated the trARPES measurements above the equilibrium transition temperature at $T = 110\,\mathrm{K} > T_{CDW}$ and observed a uniform metallic response throughout the band structure (*SI Appendix*). A recent classification of the bands that host the CDW gap in CsV_3Sb_5 shows consistent results with Fig. 2 *D*–*F*, distinguishing between three bands of which two host a substantial gap (42).

Next, we extract the spectral intensity in specific regions of interest (see rectangles in Fig. 2*D*) at the top of the Γ and M bands (E = − 20 meV) and in the excited states region (E = 130 meV) at the M point as a function of time delay (Fig. 2*G*). Due to their prompt excitation and short lifetime, we identify the temporal overlap (t_0) of the pump and probe with the peak of the excited states signal. Clearly, the response at the M point and Γ band below E_F is very different—the metallic band around the Γ point is depleted nearly instantaneously, whereas inside the gap at the M point, we detect an intensity increase. The long-lived depletion at the Γ band can most likely be related to the limited recombination channels for this particular band (*SI Appendix*), similarly seen as an anomalously long recovery behavior in time-resolved reflectivity measurements (28). The in-gap intensity decays in about 4 ps, indicating that the CDW gap reopens on a similar timescale as observed in other compounds (43). Fig. 2*H* shows a zoom-in around $\Delta t = 0$ to better visualize the behavior during the photoexcitation. The excited states at the M point (turquoise) show a fast rise, synchronized with the depletion peak of the Γ band. By contrast, the in-gap intensity clearly shows a 250-fs delayed response compared to the peak in the excited states, providing a direct measurement of the nonthermal CDW melting time. As we increase the pump fluence, we observe a slight increase of the melting time (Fig. 2*I*). Previous studies of other systems used a discriminatory approach (44), based on the CDW melting time, to distinguish between CDWs dominated by either electron–electron or electron–phonon interactions. A key ingredient to this approach is the comparison between the melting time and the fundamental time scale imposed by the dominant interaction, which can range between a few (electronic) to hundreds (structural) of fs. For example, the electronically driven CDW in $1T - TiSe_2$ was observed to melt within about 40 fs (33), while the structural CDW in $1T - TaS_2$ melts within 230 fs (44). Importantly, in these pioneering works, it has been shown that the melting time for electronically driven CDW decreases as the pump fluence and, therefore, the density of photo-excited carriers increases. The measured melting time as well as its fluence dependence in CsV_3Sb_5 points toward electron–phonon interactions dominating the CDW in CsV_3Sb_5, as it corresponds to the typical time scale of atomic motion in a solid. Nevertheless, a complete determination of the CDW mechanism is only possible with precise knowledge of a reference time frame, i.e., the time it takes for the atoms to move back to their undistorted arrangement. This time-scale is given by the amplitude mode frequency Ω_Δ, which so-far eluded detection in CsV_3Sb_5 (22, 27–30).

This missing information can be retrieved by examining the coherent oscillations which are superimposed on our time-resolved spectral intensity signal. We make use of our momentum resolution to examine these band-selective oscillations at specific high-symmetry points of the Brillouin zone. Fig. 3 *A*, *C*, and *E* show the transient spectral intensity change of the bands close to Γ, K, and M just below E_F. A Fourier analysis of the coherent oscillations reveals well-separated peaks above the noise floor of the experiment. Most strikingly, the distinct bands at Γ, K and M show different oscillation frequencies (Fig. 3 *B*, *D*, and *F*). We note that the intensity increase at negative delays are due to a pump-polarization-dependent space charge effect, which does not affect the positive delay signal (see *SI Appendix* for details). A comparison with previous Raman (27) and coherent phonon spectroscopy (28) measurements, shows good agreement between the detected oscillation frequencies at Γ and K and the reported phonon modes of CsV_3Sb_5 (Fig. 3*G*). Importantly, all common phonon modes that appear in both Raman and our trARPES measurements are associated with the CDW phase transition. We further find good agreement with frozen-phonon DFT calculations which predict pronounced electron–phonon coupling to the high-symmetry points of the electronic band structure (*SI Appendix*). Interestingly, an equivalent analysis of the in-gap intensity at the M point reveals two collective modes at 1.6 THz and 2.4 THz (Fig. 3*F*), which do not appear in any static or time-resolved measurement. These modes do not overlap with any of the phonon modes observed at other momentum points (Fig. 3 *B* and *D*). Finally, a fluence-dependent measurement reveals a pronounced softening of these two modes, in stark contrast to the phonons, which hardly respond to the pump fluence variation (Fig. 3*H*). These observations prompt the question of the origin of these in-gap modes.

Discussion

We recall that the amplitude mode renormalizes the size of the CDW gap and can consequently be observed as coherent oscillations of the in-gap intensity (45). Thus, the measured oscillations at the M point can, in principle, be assigned to coherent oscillations of the amplitude mode. Yet, the observation of two modes modulating the in-gap intensity cannot be reconciled with amplitude oscillations of a single complex order parameter. Recent studies have shown that the out-of-plane lattice reconstruction consists of alternating SOD and iSOD distortions on adjacent layers (46, 47) (Fig. 1*B*). Therefore, in the limit of vanishing coupling between the layers, one can regard the three-dimensional CDW as a superlattice of stacked SOD and iSOD CDWs each with their individual order parameter and set of collective modes. Indeed, recent x-ray diffraction measurements reveal that the 3-D structure is very amenable to perturbation suggesting only weak coupling between the layers (48). As outlined above, our photoexcitation quenches

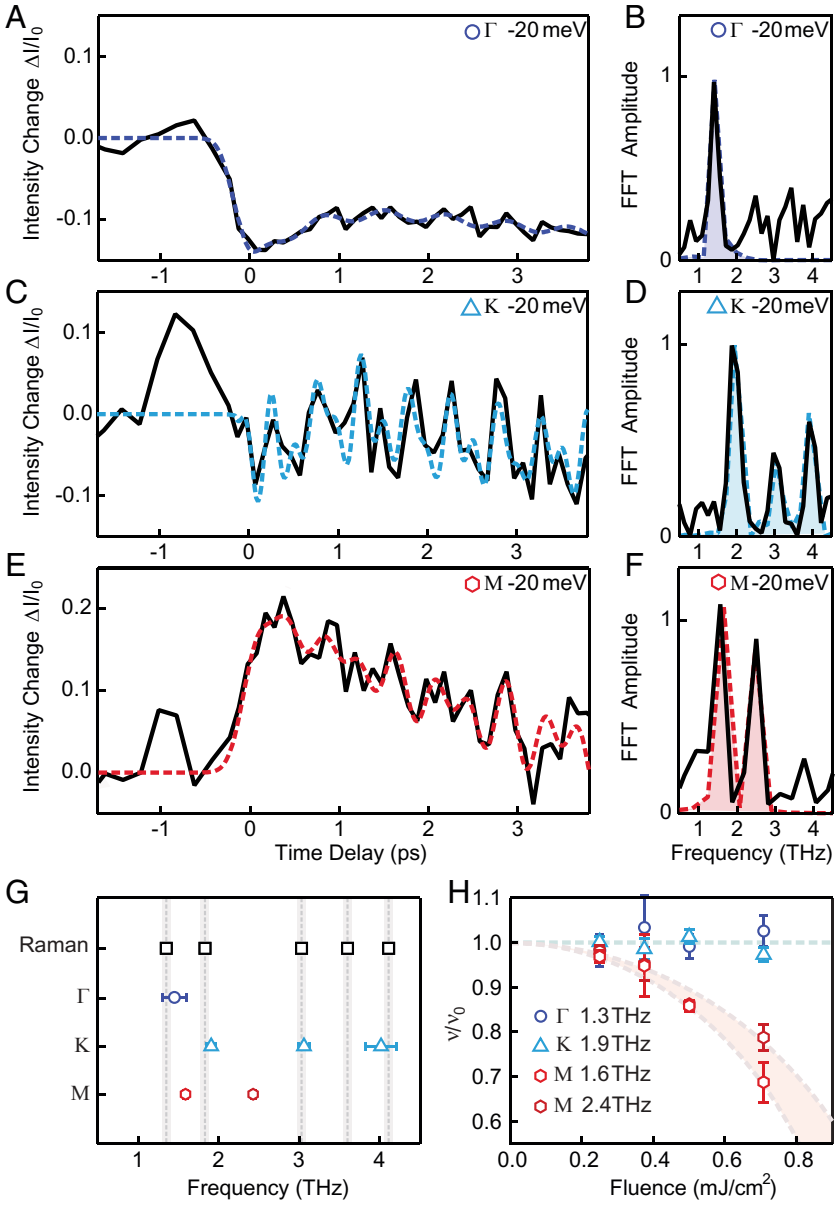

Fig. 3. Coherent phonons and charge density wave collective modes in CsV_3Sb_5. (*A*–*D*) Time-resolved intensity change at the Γ (*A*) and K (*C*) bands for an excitation fluence of 0.5 mJ/cm^2. The black line is the raw data and the dashed line is a fit to the data (*SI Appendix*). (*B*) and (*D*) show Fourier intensity of the raw signal, after subtracting the slowly varying background. The Fourier intensity of the oscillatory part of the fit in (*A*) and (*C*) is presented as well (dashed line). (*E* and *F*) In-gap Intensity change as a function of time delay also for an excitation fluence of 0.5 mJ/cm^2. The same analysis as in (*A*) and (*C*) reveals two dominant frequencies, at 1.6 THz and 2.4 THz. For (*A*), (*C*), and (*E*), the integration range over momentum (0.07 Å^{-1}) and energy (30 meV) is indicated by the rectangles in Fig. 2 *A* and *D*. (*G*) Comparison between the frequencies of the coherent oscillations at the high-symmetry points and known Raman phonons (27). The coherent modes at the K and Γ bands agree well with the Raman modes that appear below T_{CDW}. The coherent modes at M do not coincide with any known Raman mode. (*H*) Relative frequency shift of the 1.9-THz and 1.3-THz phonon mode and the in-gap modes as a function of pump fluence. The phonon modes' frequency remains constant while the in-gap modes show softening. The dashed lines are a guide to the eye, and the error bars correspond to the uncertainties of the time-domain fit.

the CDW and accordingly suppresses the weak coupling among the SOD and iSOD distorted layers allowing them to perform amplitude oscillations at their own eigenfrequencies. To estimate these frequencies, we calculated the free energy for the two distortions using DFT methods, which allowed us to extract the two associated amplitude mode frequencies (see Fig. 4 and *SI Appendix*) $\nu_{SOD} = 3.2$ THz and $\nu_{iSOD} = 4.6$ THz for the SOD and iSOD distortions, respectively. These calculations are done at $T = 0$ and do not include anharmonicity effects as well as complex trajectories of the atoms, and accordingly represent a maximum value of the frequencies (see *SI Appendix* for details). However, the ratio $\alpha = \nu_{iSOD}/\nu_{SOD}$ of the two frequencies is minimally affected by these uncertainties, as they affect all collective oscillations in the same manner, and we therefore use it as a quantitative metric to compare with our experimental result. Considering the complex lattice and electronic structure of CsV_3Sb_5, we find surprisingly good agreement between the experimental $\alpha = 1.5 \pm 0.1$ and theoretical $\alpha = 1.4$ frequency ratio. Therefore, we find that the coherent oscillations within the gap can be ascribed to independent amplitude oscillations of the SOD and iSOD layers. In principle, each distortion type generates a specific energy gap; however, since the distortion magnitude is very similar in both cases (Fig. 4), their associated gaps are almost degenerate (*SI Appendix*), and therefore cannot

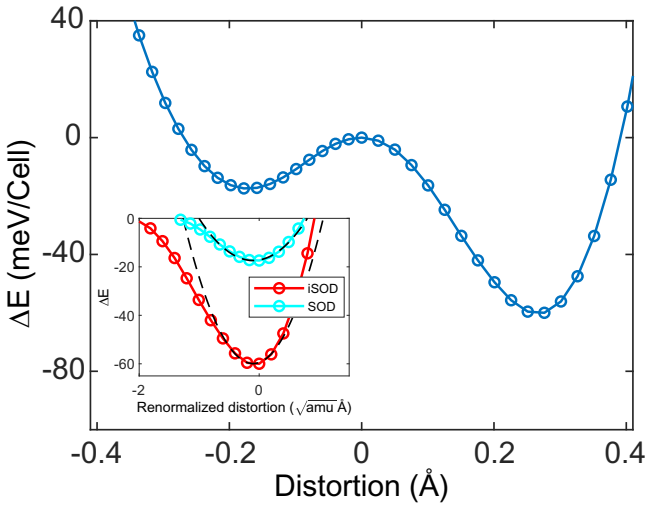

Fig. 4. Total energy profiles for SOD and iSOD distortions. DFT calculation of the total energy difference for the SOD (negative side) and iSOD (positive side) distortions in CsV_3Sb_5 with respect to the pristine structure. The distortion parameter is defined by Eq. **1** in *SI Appendix*. (*Inset*) The mass-weighted distortion–energy relation to extract the collective oscillation frequency by Eq. **2** in *SI Appendix*. Parabolic fits are shown in dashed black.

be resolved independently within our measurement energy resolution. Our findings can offer a possible reason for the absence of the amplitude modes in Raman measurements. The structural distortions associated with the amplitude modes of the alternating SOD and iSOD layers are exactly the opposite of each other and, while the layers are coupled in equilibrium, may therefore render this mode silent for a typical Raman experiment. Our trARPES experiment on the other hand is directly sensitive to changes of the CDW gap and therefore allows us to identify the amplitude modes according to their coherent beating pattern. These modes provide the fastest possible time scale for the structural reconfiguration of a CDW—melting cannot occur faster than half of an oscillation cycle $T_\Delta = \frac{1}{\nu_\Delta}$ of the amplitude mode. Accordingly, we compare the amplitude mode frequencies of the two distortions and we find $T_\Delta/2 \approx 200$ fs and 300 fs for the SOD and iSOD distortions, respectively. This result is in excellent agreement with the observed melting time $\tau \approx 250$ fs and clearly set electron–phonon interactions as the dominant mechanism that drives the CDW in CsV_3Sb_5.

Apart from clarifying important aspects of the CDW order itself, the collective excitations in the low THz-regime presented here may be furthermore valuable in understanding the superconducting phase in CsV_3Sb_5 which develops below $T = 3$ K. The superconducting order parameter is believed to form a commensurate pair density wave, possibly of unconventional origin (8), and the phase diagram both as a function of doping (48) and pressure (13, 49) strongly suggests that the emergence of superconductivity is linked to the parent CDW phase, and might even compete with it. As CsV_3Sb_5 does not feature any magnetic order, the collective excitations associated with the CDW are therefore a prime candidate for the possible pairing glue if the superconducting instability is unconventional. Based on our findings, we believe that a detailed analysis of this possibility is called for.

To conclude, we have used trARPES to study the CDW in CsV_3Sb_5 and observed its nonthermal melting and recovery. From this time-resolved measurement, we were able to extract the CDW melting time and identify coherent oscillations of the CDW amplitude mode, which provide a complete basis to identify the dominant interaction in the CDW phase. We find that the observed melting time of $\tau \approx 250$ fs, together with amplitude mode frequencies of 2-3 THz, is evidence that the CDW phase is dominated by electron–phonon interactions. This strong evidence of a structural nature of the CDW in CsV_3Sb_5 unambiguously demonstrates the important role the crystal lattice plays in a system that is believed to be dominated by electronic correlations (4, 18–23).

Materials and Methods

trARPES. We use a high-energy fiber laser system with a fundamental wavelength of 1,030 nm, repetition rate of 300 KHz, pulse duration of 130 fs, and pulse energy of 165 mJ for generating the pump and probe beams. For the probe beam, we generate the second harmonic of the fundamental beam, and focus it into a continuous flow argon gas jet within a vacuum system, in order to generate high harmonics. In our measurements, we use the 11th harmonic (26.4 eV), with linear polarization aligned out-of-plane with respect to the sample surface (the angle of incidence of the beams is about 45°). For the pump beam, we either use the fundamental beam, or the output of an optical parametric oscillator. Finally, the pump–probe pair are spatially and temporally overlapped on the sample surface, where their synchronization is controlled via a delay scanning stage (with measured temporal resolution of 110 fs, see *SI Appendix*). The ARPES measurements are based on a time-of-flight detector (Scienta Omicron), that allows simultaneous detection of both in-plane momenta and kinetic energy, with 0.01 $Å^{-1}$ and 60 meV momentum and energy resolution, respectively. CsV_3Sb_5 single crystals were cleaved after cooling down in an ultrahigh vacuum chamber with base pressure $< 6 \times 10^{-11}$ torr.

Crystal Synthesis. Synthesis of single crystal samples of CsV_3Sb_5 was performed by the self-flux method. Elemental Cs (liquid, Alfa 99.98%), V (powder, Sigma 99.9%), and Sb (shot, Alfa 99.999%) were milled in a tungsten carbide vial under an argon environment in a eutectic mixture of CsSb and Cs_3Sb_7 with VSb_2. The vanadium powder was purified with a mixture of concentrated HCl and EtOH prior to being added to the mixture. The resulting flux powder was then loaded into alumina crucibles and sealed inside steel tubes. The samples were then heated up to 1,000 °C, soaked at that temperature for 24 h and cooled down to 600 °C at 2 °C/h. Once cooled, crystals were extracted manually in air.

DFT Calculations. All calculations are performed with density-functional theory as implemented in Vienna ab-initio Simulation Package (*VASP*) (50). The generalized gradient approximation as parameterized by Perdew–Burke–Ernzerhof is employed (51). The cutoff energy for the plane-wave basis set is 300 eV. Phonon bands are calculated with the finite displacement method as implemented in PHONOPY software (52).

Data, Materials, and Software Availability. All study data are included in the article and/or *SI Appendix*.

ACKNOWLEDGMENTS. We thank Dongsung Choi, Baiqing Lyu, and Masataka Mogi for technical support. The work at MIT was supported by the US Department of Energy, BES DMSE (data taking, analysis, and manuscript writing) and Gordon and Betty Moore Foundation's EPiQS Initiative grant GBMF9459 (instrumentation). D.A. acknowledges financial support by the Zuckerman STEM Leadership Program. A.v.H. gratefully acknowledges funding by the Humboldt Foundation. B.Y. acknowledges the financial support by the European Research Council (ERC Consolidator Grant "NonlinearTopo," No. 815869) and the ISF–Personal Research Grant (No. 2932/21). S.D.W., B.R.O., and A.C.S. gratefully acknowledge support via the UC Santa Barbara NSF Quantum Foundry funded via the Q-AMASE-i program under award DMR-1906325.

Author affiliations: [a]Department of Physics, Massachusetts Institute of Technology, Cambridge, MA 02139; [b]Department of Condensed Matter Physics, Weizmann Institute of Science, Rehovot 7610001, Israel; and [c]Materials Department, University of California, Santa Barbara, CA 93106

1. E. Fradkin, S. A. Kivelson, J. M. Tranquada, Colloquium: Theory of intertwined orders in high temperature superconductors. *Rev. Mod. Phys.* **87**, 457 (2015).
2. B. R. Ortiz *et al*., New kagome prototype materials: Discovery of KV_3Sb_5, RbV_3Sb_5, and CsV_3Sb_5. *Phys. Rev. Mater.* **3**, 094407 (2019).
3. B. R. Ortiz *et al*., Fermi surface mapping and the nature of charge-density-wave order in the kagome superconductor CsV_3Sb_5. *Phys. Rev. X* **11**, 041030 (2021).
4. Y.-X. Jiang *et al*., Unconventional chiral charge order in kagome superconductor KV_3Sb_5. *Nat. Mater.* **20**, 1353–1357 (2021).
5. Z. Liang *et al*., Three-dimensional charge density wave and surface-dependent vortex-core states in a kagome superconductor CsV_3Sb_5. *Phys. Rev. X* **11**, 031026 (2021).
6. B. R. Ortiz *et al*., CsV_3Sb_5: A Z_2 topological kagome metal with a superconducting ground state. *Phys. Rev. Lett.* **125**, 247002 (2020).
7. H. Zhao *et al*., Cascade of correlated electron states in the kagome superconductor CsV_3Sb_5. *Nature* **599**, 216–221 (2021).
8. H. Chen *et al*., Roton pair density wave in a strong-coupling kagome superconductor. *Nature* **599**, 222–228 (2021).
9. B. R. Ortiz *et al*., Superconductivity in the Z_2 kagome metal KsV_3Sb_5. *Phys. Rev. Mater.* **5**, 034801 (2021).
10. Q. Wang *et al*., Charge density wave orders and enhanced superconductivity under pressure in the kagome metal CsV_3Sb_5. *Adv. Mater.* **33**, 2102813 (2021).
11. Y. Hu *et al*., Rich nature of Van Hove singularities in Kagome superconductor CsV_3Sb_5. *Nat. Commun.* **13**, 1–7 (2022).
12. F. Du *et al*., Pressure-induced double superconducting domes and charge instability in the kagome metal KV_3Sb_5. *Phys. Rev. B* **103**, L220504 (2021).
13. K. Y. Chen *et al*., Double superconducting dome and triple enhancement of T_c in the kagome superconductor CsV_3Sb_5 under high pressure. *Phys. Rev. Lett.* **126**, 247001 (2021).
14. F. Yu *et al*., Unusual competition of superconductivity and charge-density-wave state in a compressed topological kagome metal. *Nat. Commun.* **12**, 1–6 (2021).
15. Y. M. Oey, F. Kaboudvand, B. R. Ortiz, R. Seshadri, S. D. Wilson, Tuning charge density wave order and superconductivity in the kagome metals $KV_3Sb_{5-x}Sn_x$ and $RbV_3Sb_{5-x}Sn_x$. *Phys. Rev. Mater.* **6**, 074802 (2022).
16. Q. Stahl *et al*., Temperature-driven reorganization of electronic order in CsV_3Sb_5. *Phys. Rev. B* **105**, 195136 (2022).
17. Q. Xiao *et al*., Coexistence of multiple stacking charge density waves in kagome superconductor CsV_3Sb_5. arXiv [Preprint] (2022). http://arxiv.org/abs/2201.05211 (Accessed 27 January 2022).
18. N. Shumiya *et al*., Intrinsic nature of chiral charge order in the kagome superconductor RbV_3Sb_5. *Phys. Rev. B* **104**, 035131 (2021).
19. Z. Wang *et al*., Electronic nature of chiral charge order in the kagome superconductor CsV_3Sb_5. *Phys. Rev. B* **104**, 075148 (2021).
20. H. Li *et al*., Observation of unconventional charge density wave without acoustic phonon anomaly in kagome superconductors AV_3Sb_5 (A= Rb, Cs). *Phys. Rev. X* **11**, 031050 (2021).
21. F. Yu *et al*., Concurrence of anomalous Hall effect and charge density wave in a superconducting topological kagome metal. *Phys. Rev. B* **104**, L041103 (2021).
22. G. Liu *et al*., Observation of anomalous amplitude modes in the kagome metal CsV_3Sb_5. *Nat. Commun.* **13**, 1–8 (2022).
23. S.-Y. Yang *et al*., Giant, unconventional anomalous Hall effect in the metallic frustrated magnet candidate, KV_3mSb_5. *Sci. Adv.* **6**, eabb6003 (2020).
24. Y. Zhu *et al*., Unconventional slowing down of electronic recovery in photoexcited charge-ordered $La_{1/3}Sr_{2/3}FeO_3$. *Nat. Commun.* **9**, 1–7 (2018).
25. A. Zong *et al*., Evidence for topological defects in a photoinduced phase transition. *Nat. Phys.* **15**, 27–31 (2019).
26. A. Zong *et al*., Dynamical slowing-down in an ultrafast photoinduced phase transition. *Phys. Rev. Lett.* **123**, 097601 (2019).
27. S. Wu *et al*., Charge density wave order in the kagome metal AV_3Sb_5 (A= Cs, Rb, K). *Phys. Rev. B* **105**, 155106 (2022).
28. N. Ratcliff, L. Hallett, B. R. Ortiz, S. D. Wilson, J. W. Harter, Coherent phonon spectroscopy and interlayer modulation of charge density wave order in the kagome metal CsV_3Sb_5. *Phys. Rev. Mater.* **5**, L111801 (2021).
29. Z. X. Wang *et al*., Unconventional charge density wave and photoinduced lattice symmetry change in the kagome metal CsV_3Sb_5 probed by time-resolved spectroscopy. *Phys. Rev. B* **104**, 165110 (2021).
30. Q. Wu *et al*., Simultaneous formation of two-fold rotation symmetry with charge order in the kagome superconductor CsV_3Sb_5 by optical polarization rotation measurement. *Phys. Rev. B* **106**, 205109 (2022).
31. L. Perfetti *et al*., Time evolution of the electronic structure of 1T-TaS_2 through the insulator-metal transition. *Phys. Rev. Lett.* **97**, 067402 (2006).
32. F. Schmitt *et al*., Transient electronic structure and melting of a charge density wave in $TbTe_3$. *Science* **321**, 1649–1652 (2008).
33. T. Rohwer *et al*., Collapse of long-range charge order tracked by time-resolved photoemission at high momenta. *Nature* **471**, 490–493 (2011).
34. S.-L. Yang *et al*., Mode-selective coupling of coherent phonons to the Bi2212 electronic band structure. *Phys. Rev. Lett.* **122**, 176403 (2019).
35. S. Gerber *et al*., Femtosecond electron-phonon lock-in by photoemission and X-ray free-electron laser. *Science* **357**, 71–75 (2017).
36. S. Sakamoto, N. Gauthier, P. S. Kirchmann, J. A. Sobota, Z.-X. Shen, Connection between coherent phonons and electron-phonon coupling in Sb (111). *Phys. Rev. B* **105**, L161107 (2022).
37. Z. Wang *et al*., Distinctive momentum dependent charge-density-wave gap observed in CsV_3Sb_5 superconductor with topological Kagome lattice. arXiv [Preprint] (2021). http://arxiv.org/abs/2104.05556 (Accessed 24 January 2022).
38. K. Nakayama *et al*., Multiple energy scales and anisotropic energy gap in the charge-density-wave phase of the kagome superconductor CsV_3Sb_5. *Phys. Rev. B* **104**, L161112 (2021).
39. Y. Luo *et al*., Distinct band reconstructions in kagome superconductor CsV_3Sb_5. arXiv [Preprint] (2021). http://arxiv.org/abs/2106.01248 (Accessed 27 January 2022).
40. R. Lou *et al*., Charge-density-wave-induced peak-dip-hump structure and the multiband superconductivity in a kagome superconductor CsV_3Sb_5. *Phys. Rev. Lett.* **128**, 036402 (2022).
41. J. Maklar *et al*., Nonequilibrium charge-density-wave order beyond the thermal limit. *Nat. Commun.* **12**, 1–8 (2021).
42. M. Kang *et al*., Twofold van Hove singularity and origin of charge order in topological kagome superconductor CsV_3Sb_5. *Nat. Phys.* **18**, 301–308 (2022).
43. M. Eichberger *et al*., Snapshots of cooperative atomic motions in the optical suppression of charge density waves. *Nature* **468**, 799–802 (2010).
44. S. Hellmann *et al*., Time-domain classification of charge-density-wave insulators. *Nat. Commun.* **3**, 1–8 (2012).
45. G. Grüner, The dynamics of charge-density waves. *Rev. Mod. Phys.* **60**, 1129 (1988).
46. M. Kang *et al*., Charge order landscape and competition with superconductivity in kagome metals. *Nat. Mater.* **22**, 186–193 (2023).
47. C. Li *et al*., Coexistence of two intertwined charge density waves in a kagome system. *Phys. Rev. Res.* **4**, 033072 (2022).
48. L. Kautzsch *et al*., Incommensurate charge-stripe correlations in the kagome superconductor $CsV_3Sb_{5-x}Sn_x$. arXiv [Preprint] (2022). http://arxiv.org/abs/2207.10608 (Accessed 8 April 2022).
49. L. Zheng *et al*., Emergent charge order in pressurized kagome superconductor CsV_3Sb_5. *Nature* **611**, 682–687 (2022).
50. G. Kresse, J. Furthmüller, Efficiency of ab-initio total energy calculations for metals and semiconductors using a plane-wave basis set. *Comput. Mater. Sci.* **6**, 15–50 (1996).
51. J. P. Perdew, K. Burke, M. Ernzerhof, Generalized gradient approximation made simple. *Phys. Rev. Lett.* **77**, 3865 (1996).
52. A. Togo, I. Tanaka, First principles phonon calculations in materials science. *Scr. Mater.* **108**, 1–5 (2015).